PHOTONICS Research

Generating a nanoscale blade-like optical field in a coupled nanofiber pair

Yuxin Yang,[1,†] Jiaxin Gao,[1,†] Hao Wu,[1] Zhanke Zhou,[1] Liu Yang,[1] Xin Guo,[1,2,4] Pan Wang,[1,2] and Limin Tong[1,2,3,5]

[1]Interdisciplinary Center for Quantum Information, New Cornerstone Science Laboratory, State Key Laboratory of Extreme Photonics and Instrumentation, College of Optical Science and Engineering, Zhejiang University, Hangzhou 310027, China
[2]Jiaxing Key Laboratory of Photonic Sensing & Intelligent Imaging, Intelligent Optics & Photonics Research Center, Jiaxing Research Institute Zhejiang University, Jiaxing 314000, China
[3]Collaborative Innovation Center of Extreme Optics, Shanxi University, Taiyuan 030006, China
[4]e-mail: guoxin@zju.edu.cn
[5]e-mail: phytong@zju.edu.cn
[†]These authors contributed equally to this work.

Received 22 September 2023; revised 9 November 2023; accepted 10 November 2023; posted 14 November 2023 (Doc. ID 506681); published 22 December 2023

An optical field with sub-nm confinement is essential for exploring atomic- or molecular-level light-matter interaction. While such fields demonstrated so far have typically point-like cross-sections, an optical field having a higher-dimensional cross-section may offer higher flexibility and/or efficiency in applications. Here, we propose generating a nanoscale blade-like optical field in a coupled nanofiber pair (CNP) with a 1-nm-width central slit. Based on a strong mode coupling-enabled slit waveguide mode, a sub-nm-thickness blade-like optical field can be generated with a cross-section down to ~0.28 nm × 38 nm at 1550 nm wavelength (i.e., a thickness of $\sim\lambda_0/5000$) and a peak-to-background intensity ratio (PBR) higher than 20 dB. The slit waveguide mode of the CNP can be launched from one of the two nanofibers that are connected to a standard optical fiber via an adiabatical fiber taper, in which a fundamental waveguide mode of the fiber can be converted into a high-purity slit mode with high efficiency (>98%) within a CNP length of less than 10 μm at 1550 nm wavelength. The wavelength-dependent behaviors and group velocity dispersion in mode converting processes are also investigated, showing that such a CNP-based design is also suitable for broadband and ultrafast pulsed operation. Our results may open up new opportunities for studying light-matter interaction down to the sub-nm scale, as well as for exploring ultra-high-resolution optical technology ranging from super-resolution nanoscopy to chemical bond manipulation.

https://doi.org/10.1364/PRJ.506681

1. INTRODUCTION

Due to the sub-nm feature size of typical atomic or molecular structures, the sub-nm-confined optical field is fundamentally important for exploring light-matter interaction on the bottom and pushing the limit of optical technology ranging from super-resolution nanoscopy [1–3] and molecular spectroscopy [4–6] to atom/molecule manipulation [7–9]. Current available approaches to such fields mostly rely on plasmonic field localization, by which effective field confinement down to the 1- or sub-nm (i.e., $\sim\lambda_0/1000$, where λ_0 is the vacuum wavelength) level has been successfully realized [2,4,10–15]. However, due to the high optical loss and large wave vector of an extremely confined plasmonic mode, challenges such as thermal issues (e.g., thermal noise and damage caused by optical absorption [16,17]) and momentum mismatch between the confined and outside free-space fields [18] remain. Recently, sub-nm-confined optical fields generated in slit modes of coupled-nanowire pairs have been demonstrated [19,20]. Relying on coherently polarized bound electrons between two opposite hexagonal nanowire vertex edges, a point-like field with optical confinement down to sub-nm was obtained. While such fields have typically quasi-zero-dimensional cross-sections, an optical field having higher-dimensional cross-section is expected to offer higher flexibility and/or efficiency in some circumstances, as shown in the light sheet for far-field super-resolution optical microscopy [21,22].

In this work, we propose generating a nanoscale blade-like optical field with sub-nm thickness in a coupled nanofiber pair (CNP). Similar to that in the coupled nanowire pair [20], when two nanofibers are placed in parallel with a central slit down to the 1 nm level, a TE_0-like nano-slit waveguiding mode with an extremely confined optical field can be obtained. However,

unlike a hexagonal crystalline nanowire that typically has a 1-nm-scale diameter of the corner edge, a cylindrical glass nanofiber used here has a 100-nm-scale diameter, offering the slit an additional dimension (i.e., expanding the projection of the slit from a point-like to a line-like shape in the cross-section) for confining the central field to a blade-like profile in spatial distribution of the near-field intensity.

Previously, coupled modes in a CNP with a slit size down to 1 nm level have been studied under weak coupling conditions [23–26]. However, due to the strong mode coupling feature of a CNP in such cases (e.g., both the ratio of diameter to wavelength and the slit width are small), especially that a sub-nm-confined field can be obtained only in a slit waveguiding mode generated by strong mode coupling of the waveguiding modes of individual nanofibers, weak coupling approximation is not suitable in such cases.

Here, under the strong coupling condition, we investigate the slit waveguiding mode in a CNP and demonstrate a sub-nm thickness blade-like field around the slit region for the first time. The peak-to-background intensity ratio (PBR) of the confined field, fiber coupling scheme, modal field evolution, and waveguide dispersion are also studied.

2. RESULTS AND DISCUSSION

A. Configuration of the CNP

The configuration of the CNP and the waveguiding nano-slit mode are schematically illustrated in Fig. 1(a). The CNP is formed by placing a pair of nanofibers closely in parallel. One end of the CNP having a flat end face is used as the output face, and the other end with one nanofiber connecting to a standard fiber (through a fiber taper) serves as the input port. The light input from the standard fiber is adiabatically transmitted through the fiber taper, coupled into the CNP waveguide, and finally converted into a TE_0-like nano-silt mode as a result of strong mode coupling between fundamental modes of the two individual nanofibers (i.e., HE_{11} modes). Relying on the coupled oscillation of polarized bound electrons around both sides of the slit, the nano-slit mode can provide a blade-like optical field with a high PBR in the cross-section of the CNP [Fig. 1(b)].

Practically, benefitting from sub-nanometer roughness of a glass nanofiber surface [27,28] that is similar to that of melt formed glass surface [29,30], when two nanofibers are assembled in close contact in parallel, the CNP can naturally form a central slit ~1 nm in width. Meanwhile, material-rich nanofibers with high refractive indices and negligible absorption loss, such as As_2S_3 glass nanofiber from near- to mid-infrared bands and SiO_2 glass nanofiber from ultraviolet to near-infrared bands, can be used to support the nano-slit mode in a wide spectral range. Also, it is worth mentioning that, in recent years, high-quality nanofibers have been reported for ultra-low-loss [31–33] and high-power optical waveguiding [34], making it possible to generate nanoscale blade-like optical fields with high peak power.

B. Nanoscale Blade-Like Optical Fields in Waveguiding Nano-Slit Modes

Generally, we use commercial software of Maxwell's equations solver (Lumerical FDTD and COMSOL) to simulate mode evolutions in the CNP in three dimensions. Here, to obtain the spatial distribution of the nano-slit modes at the output end of the CNP with high precision, we mesh the area around the nano-slit with a minimum size of 0.01 nm. To avoid an intolerable amount of computation in the 3D simulation, we used a 2D-COMSOL simulation to calculate the field distribution in an As_2S_3 glass CNP with wavelength (λ)-dependent refractive index (n) of the As_2S_3 glass shown in Fig. 6 (Appendix A). As a more precise approximation, we assume a V-shaped linearly changing index profile across the slit (Fig. 7 in Appendix A), while providing typical results calculated with a step-index profile for reference (Figs. 7 and 8 in Appendix A).

For an individual nanofiber, the fundamental mode is an HE_{11} mode. When the two nanofibers are placed in parallel and close contact, strong mode coupling occurs. Since the diameter of the nanofibers discussed here is relatively small, we plot only the lowest four eigenmodes. The spatial distribution of normalized electric field vectors and surface polarized bound charge density of the four lowest modes in an As_2S_3 CNP with a nanofiber diameter (D) of 200 nm and a slit width (W) of 1 nm at 640 nm wavelength are shown in

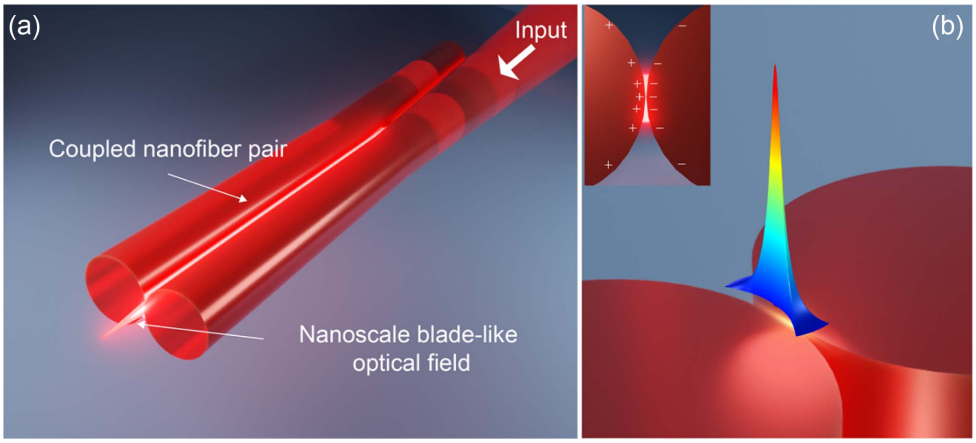

Fig. 1. (a) Schematic illustration of generating a nanoscale blade-like optical field in a CNP. (b) Close-up profile of the field around the slit in (a). The inset illustrates cross-sectional distribution of the polarized charge density.

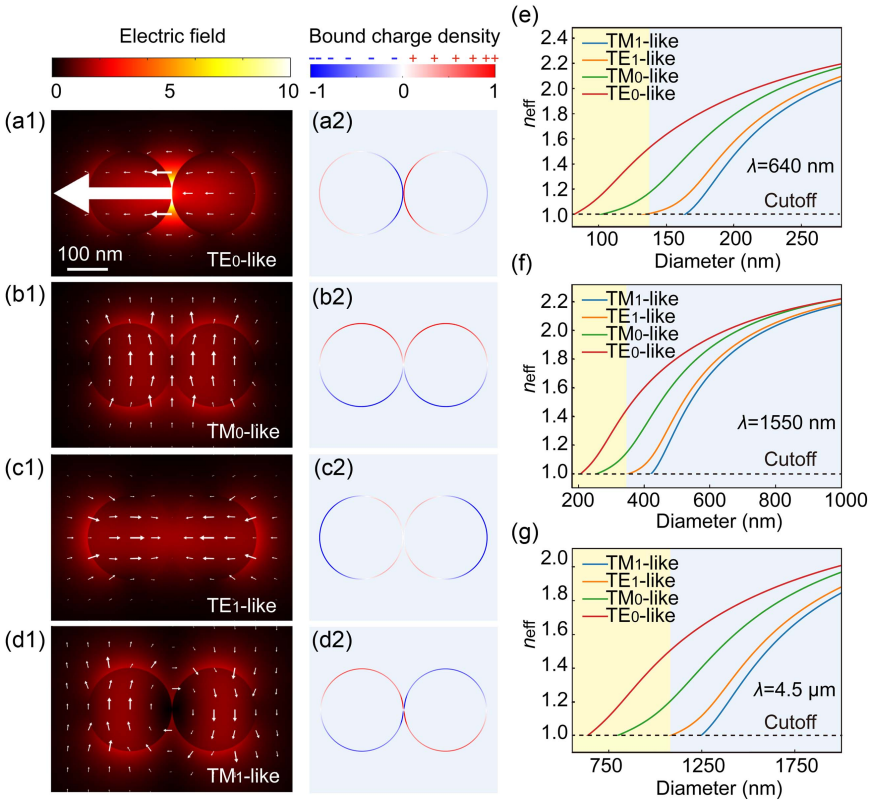

Fig. 2. Four lowest eigenmodes of the As_2S_3 CNP waveguide. Normalized electric field distribution and surface polarized bound charge density distribution of (a) TE_0-like, (b) TM_0-like, (c) TE_1-like, and (d) TM_1-like modes in an As_2S_3 CNP with $D = 200$ nm at 640 nm wavelength, respectively. The white arrows indicate the electric field vectors of the modes. The scale bar in (a) applies to (b)–(d). (e)–(g) Diameter-dependent n_{eff} of the four lowest modes of a free-standing CNP at (e) 640 nm, (f) 1550 nm, and (g) 4.5 μm wavelength, respectively. The light-yellow-shaded areas represent the selected diameter areas in this work. The dashed black lines indicate the refractive index of the air.

Figs. 2(a)–2(d). It is worth noting that the field intensity confinement and intensity within the slit in TE_0-like mode are much higher than those in other modes (here are TM_0-, TE_1-, and TM_1-like modes), which can be attributed to the high polarized charge density with opposite signs gathered at a separation of only 1 nm [Fig. 2(a2)]. For comparison, the separations between oppositely polarized charges are much larger in the other three modes.

Benefitting from the broadband transparency of As_2S_3 glass (from 570 nm to 5 μm, shown in Fig. 6), the nano-slit mode in an As_2S_3 glass CNP can be obtained within a broad spectral range. Figures 2(e)–2(g) show D-dependent effective refractive index (n_{eff}) of the four lowest modes in the CNP at visible (640 nm), near-infrared (1550 nm), and mid-infrared (4.5 μm) wavelength. Due to the different cutoff diameter of each mode, it is possible to support TE_0-like mode only and eliminate all other modes by selecting a proper D. However, in experiment, the inaccuracy in diameter measurement [35] and the varying refractive index of the material under different waveguiding power and temperature [36,37] make it difficult to precisely determine the cutoff diameter, although choosing a larger D is easier for micromanipulation in experiment. Fortunately, the polarizations of the TE_0- and TM_0-like modes are almost orthogonal, making it possible to selectively launch the TE_0-like mode by controlling the polarization of the input fiber mode. Therefore, in the following text, we consider the CNP that supports the lowest two modes only (i.e., TE_0- and TM_0-like modes) and selectively launch the TE_0-like mode by selecting the polarization of the input mode.

Figures 3(a)–3(c) show the field intensity distribution of a typical TE_0-like mode in an As_2S_3 glass CNP with $D = 300$ nm and $W = 1$ nm at 1550 nm wavelength, in which a nanoscale blade-like optical field is clearly seen. In the central slit, the dominant peak offers an extremely tight field confinement of 0.28 nm (x axis) and 38.3 nm (y axis) in the full width at half-maximum (FWHM), with a peak intensity much higher (~24 dB) than the average intensity of the whole mode field. Besides the central dominant peak, there are two side peaks in the background field due to the dielectric noncontinuity at the edge of the CNP. For reference, Fig. 3(d) shows the two side peaks (peak2), which are 18.5 dB lower in intensity compared with the central peak (peak1). It is worth mentioning that, unlike the plasmon mode that can wholly break the diffraction limit, the TE_0-like mode here as a whole is diffraction limited with an effective mode area of about 0.5 μm^2 [$\sim 0.34(\lambda/n_{eff})^2$, $n_{eff} = 1.28$]. Despite its ultra-strong field intensity, the central peak contains only a very small fraction of the total mode power, agreeing well with the low momentum mismatch between the confined field and the free space. As shown in Figs. 3(e) and 3(f), the central peak region of the TE_0-like mode accounts for 0.036% of the effective mode area and confines 0.88% of the total power. In addition, we have

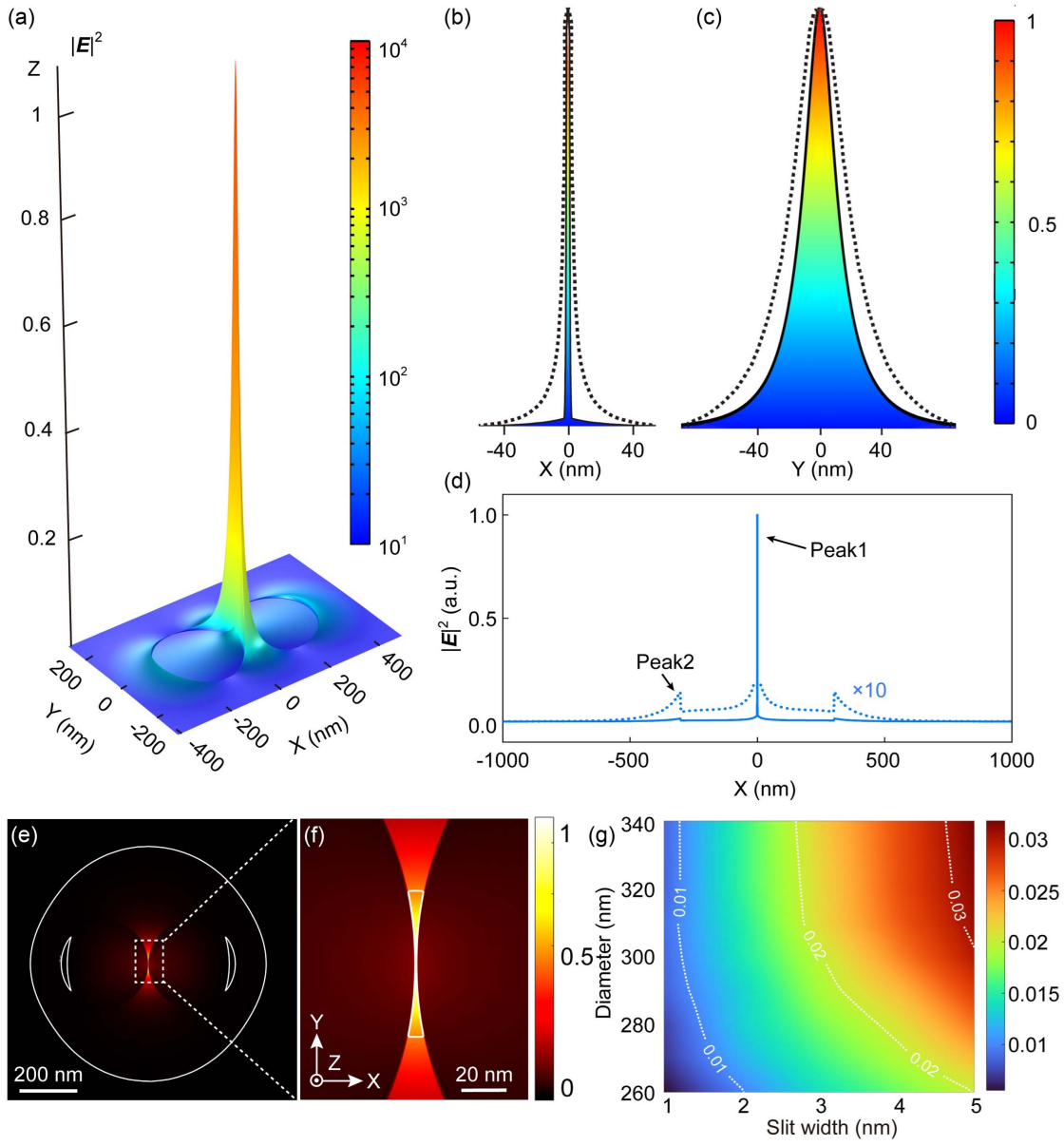

Fig. 3. Sub-nm-confined optical fields in the nano-slit mode of an As_2S_3 CNP. (a) 3D plot of the normalized cross-sectional field intensity distribution of the TE_0-like nano-slit mode of an As_2S_3 CNP with $D = 300$ nm and $W = 1$ nm at 1550 nm wavelength. (b), (c) Field intensity distribution along the horizontal (x axis) direction ($y = 0$) and the vertical (y axis) direction ($x = 0$), respectively. The dotted black lines in (b), (c) indicate the projection of spatial distribution of field intensity of the TE_0-like mode along the horizontal and the vertical direction, respectively. (d) Field intensity distribution along the x-axis direction with $y = 0$. For better clarity, a 10× profile is also plotted as dotted lines. (e) Overall distribution of Poynting vector in the z direction (P_z) around the CNP cross-section. The closed white line indicates the boundary of the effective mode area. (f) P_z distribution around the slit cross-section. The closed white line indicates the contour of $P_z(0,0)/2$, marking the profile of the central blade-like field. (g) Dependence of the fraction power in the central confined field over the total mode power on slit widths and diameters at 1550 nm wavelength.

also calculated the dependence of fractional power confined in the central peak on D and W [Fig. 3(g)], showing that the fraction of the power confined in the central peak increases with D and W.

To investigate the behavior of PBR that is critical for practical applications (e.g., a large PBR is desired to obtain a high signal-to-noise ratio), we calculated the dependence of the PBR and FWHM of the dominant peak on W and D/λ (normalized diameter) in an As_2S_3 glass CNP. Figure 4(a) gives W-dependent PBR with $D = 300$ nm at 1550 nm wavelength. It shows that, when W increases from 1 to 40 nm, the PBR decreases monotonously from 23.8 dB to 15.9 dB, while the FWHM increases monotonously from 0.28 nm (in x axis) and 38.3 nm (in y axis) to 39.4 nm (in x axis) and 119.9 nm (in y axis). Figures 4(b) and 4(c) show D/λ-dependent PBRs and FWHMs with typical D values for visible ($D = 120$ nm) and near-infrared ($D = 300$ nm) bands, respectively. The results show that, within the two cal-

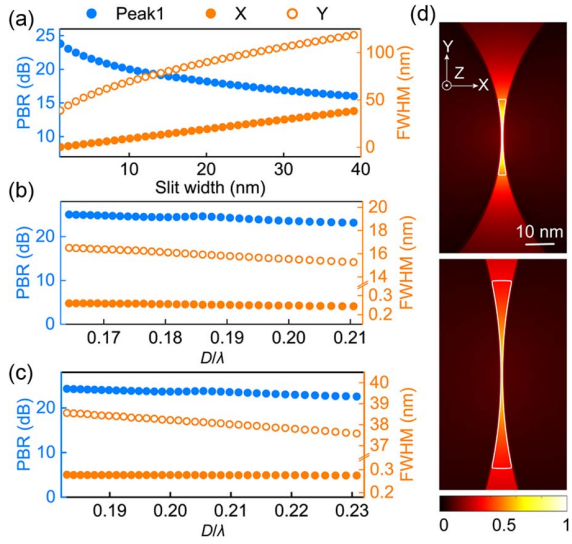

Fig. 4. (a) Slit-width-dependent PBR and FWHM of the field intensity of the TE_0-like modes in an As_2S_3 CNP with the $D = 300$ nm at 1550 nm wavelength. D/λ-dependent PBR and FWHM of the field intensity of the TE_0-like modes with $W = 1$ nm in an As_2S_3 CNP with (b) $D = 120$ nm and (c) 300 nm, respectively. (d) Cross-sectional electric field intensity of a TE_0-like mode in a CNP with $W = 1$ nm and $D = 120$ nm (up) and 300 nm (down) at 640 nm and 1550 nm wavelength, respectively. The closed white line indicates the contour of $P_z(0,0)/2$. Scale bar is 10 nm.

culated spectral ranges, when D/λ increases, the PBRs decrease slightly and the FWHMs in y axis decrease evidently, while that in the x axis keeps almost a constant (e.g., 0.28 nm with $D = 300$ nm). The large difference in FWHM and its D/λ dependence in the x and y axes offers an opportunity to generate a nanoscale blade-like field with different geometries. For example, with a similar D/λ of about 0.19 and $W = 1$ nm, a blade-like field launched by 1550 nm wavelength light with $D = 300$ nm has a y axis width (38.3 nm) twice that of the field launched by 640 nm wavelength light with $D = 120$ nm [Fig. 4(d)], while the x axis thicknesses at $y = 0$ (i.e., the minimum thickness), 0.25 nm and 0.28 nm for 640- and 1550-nm-wavelength light are very close.

C. Mode Evolution and Dispersion of Nano-Slit Modes in CNPs

As illustrated in Fig. 1(a), to simplify the launching structure, we propose using a nanofiber with one side connected to a standard fiber via a fiber taper (i.e., the nanofiber is naturally tapered down from the standard fiber). To obtain a high coupling and converting efficiency, we propose a waveguiding launching scheme including an adiabatic mode transition and side coupling with a matched effective refractive index (n_{eff}). Figure 5(a) gives a typical example of such a launching structure for 1550-nm-wavelength light with $D = 300$ nm. The input mode from a single-mode fiber (i.e., LP_{01} mode) with horizontal polarization is first converted into the nanofiber mode

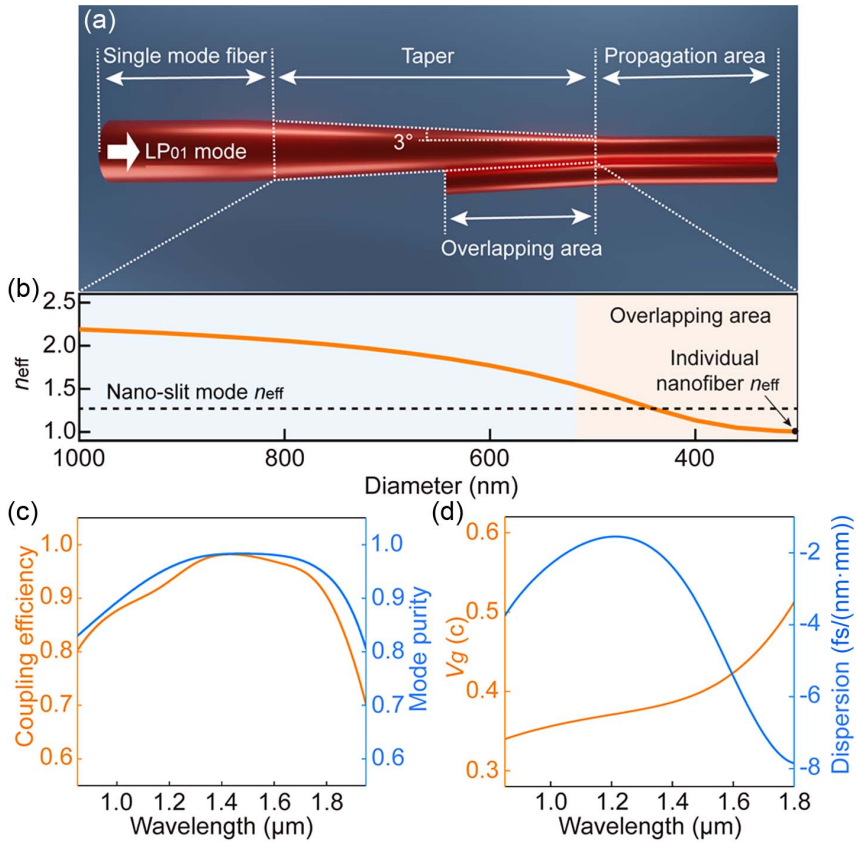

Fig. 5. (a) Schematic illustration of the coupling structure. (b) Diameter-dependent effective refractive index of As_2S_3 taper at 1550 nm wavelength. The orange-shaded area represents the overlapping area. (c) Broadband coupling efficiency and mode purity of the TE_0-like nano-slit mode in an As_2S_3 CNP with $D = 300$ nm and $W = 1$ nm. (d) Wavelength-dependent V_g and dispersion of the nano-slit mode in an As_2S_3 CNP with $D = 300$ nm and $W = 1$ nm.

(i.e., HE_{11} mode) via a fiber taper with a tapering angle of ~3° (to ensure an adiabatical mode transition [38]) and then evanescently coupled into the CNP when it reaches the overlapping area. As n_{eff} of an individual nanofiber is evidently smaller than that of the CNP, to match the n_{eff} in the evanescent coupling process, the overlapping of the second nanofiber starts from the taper region of the launching fiber [a 2-μm-length taper is long enough for ensuring an intersection point between n_{eff} of the launching fiber taper and the CNP, as shown in Fig. 5(b)]. Owing to the small diameter of the nanofiber, the slight bending of the second nanofiber can be realized by either elastic [39] or plastic [27] bending.

The light coupled into the CNP will evolve into TE_0-like nano-slit mode while propagating along the CNP. Our calculation shows that, after waveguiding through the propagation area (~7.63 μm in length) in CNP, the mode is output from the end of the CNP as a high-purity nano-slit mode. Owing to a tapering profile and thus a wide-range n_{eff} of the input fiber taper, the waveguiding scheme can be operated within a broad spectral range. For example, within about 800 nm bandwidth (from 1016 to 1870 nm wavelength), the mode purity of the nano-slit mode is higher than 90%, with a maximum of 98.3%. From 1.1 μm to 1.8 μm wavelength, the coupling efficiency of the excited nano-slit mode is higher than 90%, with a maximum efficiency approaching 98.1%, as shown in Fig. 5(c). The slight impurity may come from the forward scattering fields (due to the breakage of the symmetry of the waveguiding structure) and/or a very weak TM_0-like mode (due to the non-strictly orthogonal polarization with TE-polarized mode) that may be excited during the mode coupling and evolution processes.

Also, we investigated the group velocity (V_g) and dispersion of the TE_0-like mode around 1550 nm wavelength, as shown in Fig. 5(d). Due to the relatively small nanofiber diameter (i.e., $D \cdot n/\lambda < 1$), the increasing wavelength leads to the increasing fractional power in the air and thus increasing V_g with negative dispersion. Although the dispersion of the nano-slit mode is orders of magnitude larger than those of conventional waveguides (e.g., ~0.6 $\text{fs} \cdot \text{nm}^{-1} \cdot \text{mm}^{-1}$ at 1320 nm for single-mode fiber [40,41]), the short length of the CNP used for in-coupling and mode evolution (e.g., <10 μm) makes ultrafast pulsed operation possible. For example, after waveguiding through a 10-μm-length As_2S_3 CNP ($D = 300$ nm, $W = 1$ nm), a 100 fs pulse with a central wavelength of 1550 nm and a bandwidth of 30 nm will be broadened ~1.4 fs in pulse width.

3. CONCLUSION

In conclusion, we propose a blade-like field with sub-nanometer thickness in a waveguiding CNP. Compared with other ultra-tightly confined optical fields, such a field significantly expands its width while maintaining an extreme optical confinement in the thickness direction (i.e., 0.28 nm × 38 nm, with an aspect ratio ~100). Using a fiber taper-assisted launching scheme, the waveguiding mode from a single-mode optical fiber can be coupled into the CNP and converted into a high-purity (up to 98.3%) TE_0-like nano-slit mode with high efficiency (up to 98.1%), within a propagation length less than 10 μm at 1550 nm wavelength. In the same CNP, the TE_0-like nano-slit mode can be operated within a broad spectral range with relatively low group velocity dispersion, making it possible for ultrafast pulsed operation. Moreover, by using nanofibers with other materials (e.g., silica with lower surface roughness and shorter operation wavelength), the nano-slit can be operated with tighter confinement (see Fig. 9 in Appendix B) and/or at shorter wavelength (e.g., ultraviolet spectral range). For reference, using a CNP consisting of two 50-nm-diameter silica nanofibers, it is possible to obtain an optical confinement down to 0.15 nm at 200 nm wavelength (see Fig. 9). In addition, as the CNP reported here is a fully dielectric structure, typical issues (e.g., fluorescence quenching [42,43], Ohmic heating [17], and electron tunneling [44]) that exist in plasmonic structures will be alleviated or avoided in this case. Considering its flexibility in field generation and manipulation, such a nanoscale "optical blade" may find applications in atomic-level light-matter interaction and ultra-high-resolution optical technologies ranging from optical spectroscopy and super-resolution optical nanoscopy to chemical bond manipulation.

APPENDIX A: NUMERICAL CALCULATION

Since the CNP demonstrated here is an all-dielectric structure, its optical response can be studied using classical electromagnetic theory down to sub-nm scale [45]. Here we use commercial software of Maxwell's equations solver (Lumerical FDTD and COMSOL) to simulate mode evolutions and nano-slit modes in the CNP. Typically, the interface between the nanofiber and the air exhibits 1-nm-level surface roughness on the side edge, forming a gradual transition of the refractive index n from the glass material to the air. To simulate the nano-slit mode with enough precision, we discretize the area near the slit into triangle meshes with a minimum element size of 0.01 nm and use a linearly changing index profile from n of the bulk material (e.g., n_{As2S3} or n_{SiO2} shown in Fig. 6) to the n of the environment (e.g., n_{air}), as shown in Fig. 7(a). For comparison, we also simulate the nano-slit mode in the CNP using a step changing index profile of the interface between the nanofiber and the air [as shown in Fig. 7(b)].

It shows that the PBRs in the CNP with the same D and W obtained by the two models are almost the same, while the field confinement obtained by the linear approximation model is better than that obtained by the step approximation model [as shown in Figs. 8(a) and 8(b)]. For the CNP with 1 nm slit width, there is a difference between the two field intensity distributions in the CNP calculated by two models: one is the linear index profile, and the other one is the step index profile [as shown in Figs. 8(c) and 8(d)].

To compare the intensity of central peak with that of the surrounding field, we introduced the peak-to-background ratio, which is defined as $R_{Pi/B} = 10\log(I_{Pi}/I_B)$, where $i = 1, 2, \ldots$ is the peak index (e.g., $i = 1$ represents the central peak), I_{P1} is the field intensity of the central peak, I_{P2} is the field intensity of the second-highest peak (i.e., the highest side peak), and I_B is the averaged field intensity over the mode area, defined as $I_B = \iint_{\Omega} |E|^2 \mathrm{d}x\mathrm{d}y/\Omega$, where Ω represents the effective mode area and defined as the area of a region Σ that satisfies the following:

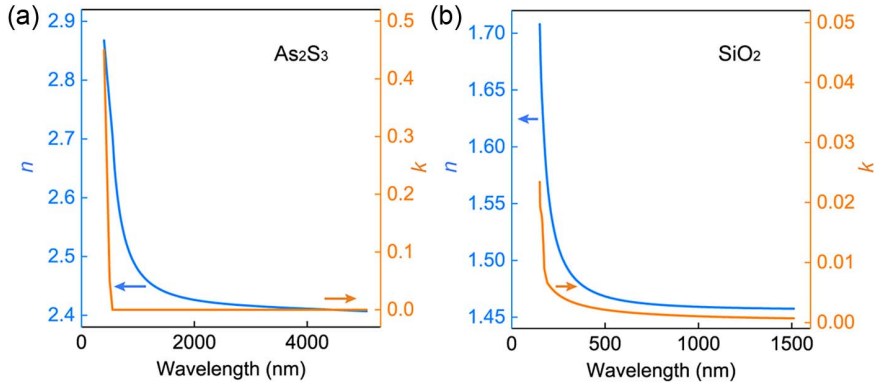

Fig. 6. Refractive indices of (a) As_2S_3 [46,47] and (b) SiO_2 [48].

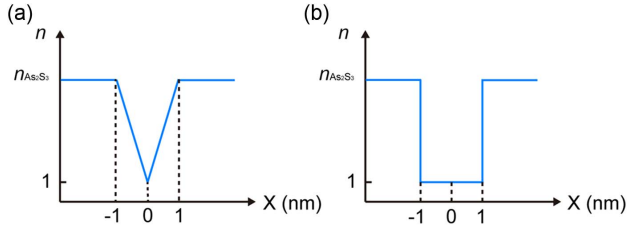

Fig. 7. Refractive index profiles of (a) linear and (b) step approximation in the silt of an As_2S_3 CNP.

(i) its boundary $\partial\Sigma$ is the contour of P_z of the mode, i.e., $P_z(\partial\Sigma)$ is constant;
(ii) 86.5% (that is $1-1/e^2$) of the total power is included inside the region, i.e.,

$$\frac{\iint_\Sigma P_z \mathrm{d}x\mathrm{d}y}{\iint P_z \mathrm{d}x\mathrm{d}y} = 1 - \frac{1}{e^2}.$$

APPENDIX B: THE WAVEGUIDING NANO-SLIT MODE IN THE SiO_2 CNP

Benefitting from the atom-level roughness of SiO_2 nanofibers (~0.25 nm [27]), the SiO_2 CNP can form a narrower slit in the center. In such a case, we investigate the TE_0-like mode of SiO_2 CNP with $W = 0.25$ nm at 200 nm wavelength ($n_{SiO2} = 1.55$). Here, we select the CNP with $D = 50$ nm that only supports the lowest two modes: TE_0-like mode and TM_0-like mode [Fig. 9(d)]. In the numerical simulation, we also use a linearly changing index profile around the 0.25-nm-thickness transitional region on the nanofiber surface (Appendix A). Figures 9(a)–9(c) give the calculated field

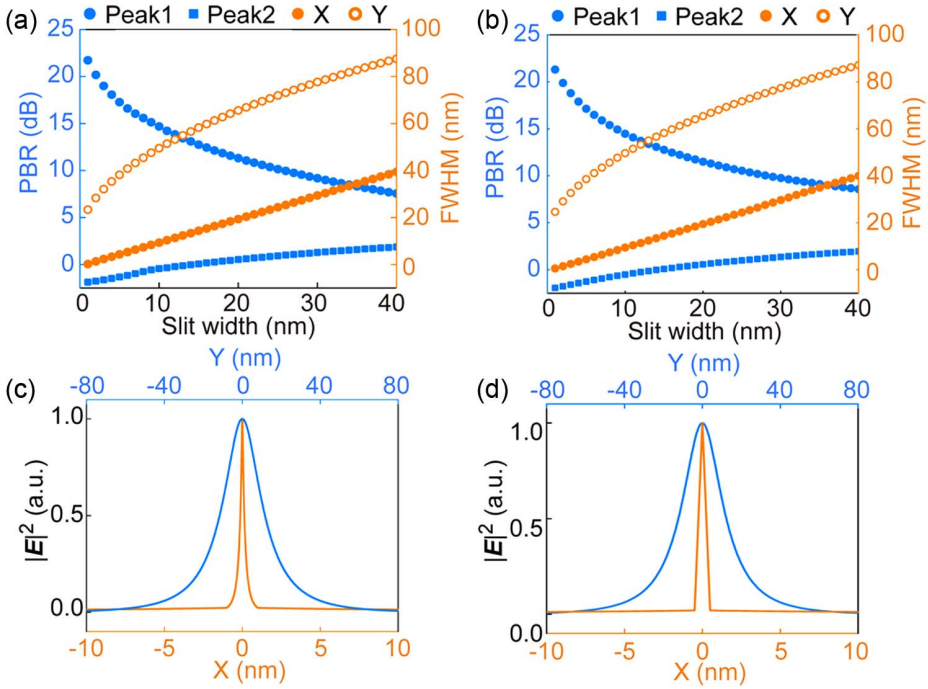

Fig. 8. Slit-width-dependent PBR and FWHM of the TE_0-like modes in an As_2S_3 CNP with $D = 200$ nm using (a) linear and (b) step approximation models at 640 nm wavelength. Field intensity distribution using the (c) linear approximation model and (d) step approximation model along the x axis with $W = 1$ nm, respectively.

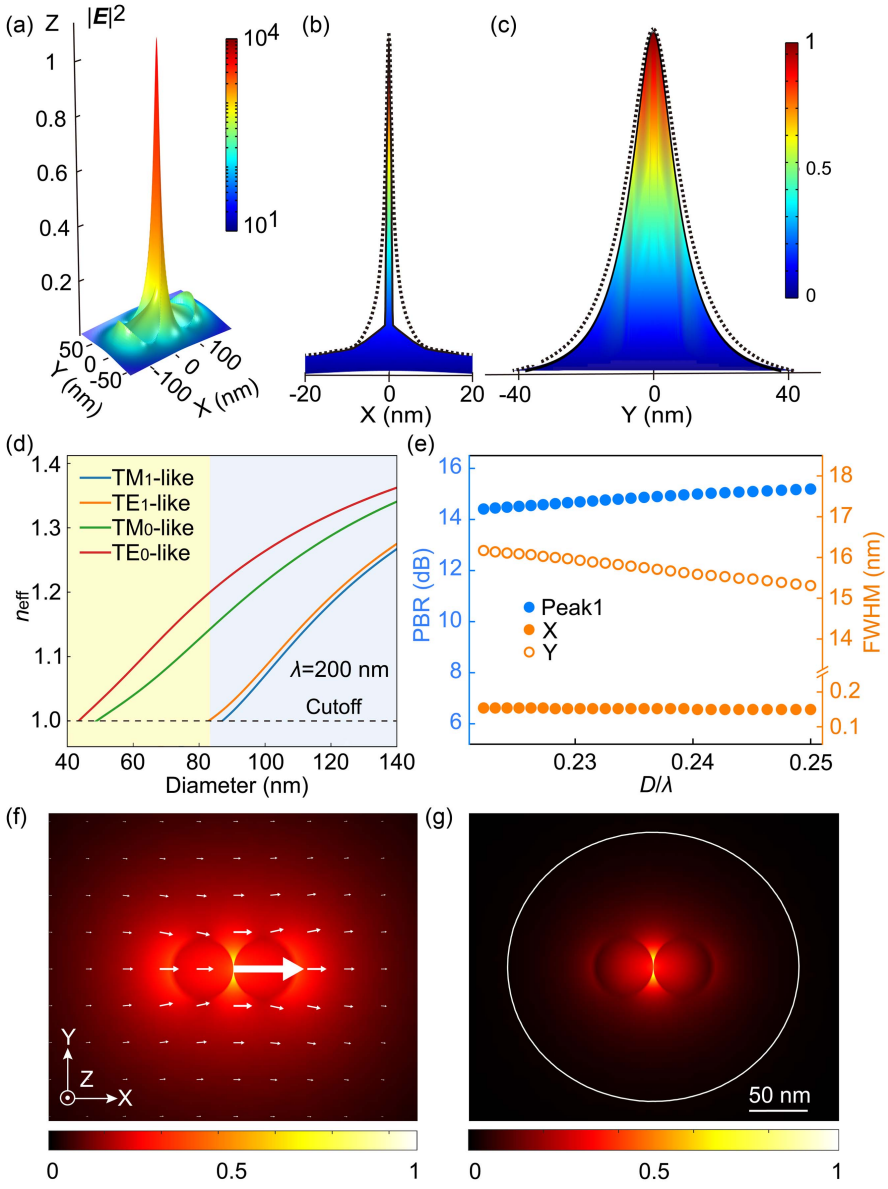

Fig. 9. Sub-nm-confined optical fields in the nano-slit mode of a SiO_2 CNP. (a) 3D plot of the normalized cross-sectional field intensity distribution of the TE_0-like nano-slit mode of a SiO_2 CNP with $D = 50$ nm and $W = 0.25$ nm at 200 nm wavelength. (b), (c) Field intensity distribution along the horizontal (x axis) direction ($y = 0$) and the vertical (y axis) direction ($x = 0$), respectively. The dotted black lines in (b), (c) indicate the projection of spatial distribution of the field intensity of the TE_0-like mode along the horizontal and the vertical direction, respectively. (d) Diameter-dependent n_{eff} of the four lowest modes of a free-standing CNP at 200 nm wavelength. (e) D/λ-dependent PBR and FWHM of the field intensity of the TE_0-like modes with $W = 0.25$ nm in a SiO_2 CNP with $D = 50$ nm. (f) Electric field vectors of the TE_0-like mode. The orientation and size of the white arrow indicate the polarization and amplitude of the local field. (g) Overall P_z distribution around the CNP cross-section. The closed white line indicates the boundary of the effective mode area.

intensity distribution of the TE_0-like mode on the end face plane of the CNP, which offers a peak field intensity around the central slit about 15.2 dB higher than the background, with an optical field confinement of 0.15 nm (x axis) and 15.3 nm (y axis) in FWHM of the field intensity [as shown in Fig. 9(e)]. Within ~0.14% of the total mode area, the ultra-confined central peak of the TE_0-like waveguiding mode in the SiO_2 nanofiber pair concentrates 1.1% of the total mode power [as shown in Figs. 9(f) and 9(g)].

Funding. New Cornerstone Science Foundation (NCI202216); National Natural Science Foundation of China (62175213, 92150302); Natural Science Foundation of Zhejiang Province (LR21F050002); Fundamental Research Funds for the Central Universities (2023QZJH27); National Key Research and Development Program of China (2018YFB2200404).

Disclosures. The authors declare no conflicts of interest.

Data Availability. The data that support the findings of this study are available from the corresponding authors upon reasonable request.

REFERENCES

1. C. Chen, N. Hayazawa, and S. Kawata, "A 1.7 nm resolution chemical analysis of carbon nanotubes by tip-enhanced Raman imaging in the ambient," Nat. Commun. **5**, 3312 (2014).
2. J. F. Schultz, L. F. Li, and S. Mahapatra, *et al.*, "Defining multiple configurations of Rubrene on a Ag(100) surface with 5 Å spatial resolution via ultrahigh vacuum tip-enhanced Raman spectroscopy," J. Phys. Chem. C **124**, 2420–2426 (2020).
3. J. Y. Xu, X. Zhu, and S. J. Tan, *et al.*, "Determining structural and chemical heterogeneities of surface species at the single-bond limit," Science **371**, 818–822 (2021).
4. R. Zhang, Y. Zhang, and Z. C. Dong, *et al.*, "Chemical mapping of a single molecule by plasmon-enhanced Raman scattering," Nature **498**, 82–86 (2013).
5. Y. Zhang, B. Yang, and A. Ghafoor, *et al.*, "Visually constructing the chemical structure of a single molecule by scanning Raman picoscopy," Natl. Sci. Rev. **6**, 1169–1175 (2019).
6. B. Yang, G. Chen, and A. Ghafoor, *et al.*, "Sub-nanometre resolution in single-molecule photoluminescence imaging," Nat. Photonics **14**, 693–699 (2020).
7. R. A. Jensen, I. C. Huang, and O. Chen, *et al.*, "Optical trapping and two-photon excitation of colloidal quantum dots using bowtie apertures," ACS Photon. **3**, 423–427 (2016).
8. A. N. Koya, J. Cunha, and T. L. Guo, *et al.*, "Novel plasmonic nanocavities for optical trapping-assisted biosensing applications," Adv. Opt. Mater. **8**, 1901481 (2020).
9. C. Zhan, G. Wang, and J. Yi, *et al.*, "Single-molecule plasmonic optical trapping," Matter **3**, 1350–1360 (2020).
10. X. Zhang, R. F. Oulton, and V. J. Sorger, *et al.*, "A hybrid plasmonic waveguide for subwavelength confinement and long-range propagation," Nat. Photonics **2**, 496–500 (2008).
11. R. F. Oulton, V. J. Sorger, and T. Zentgraf, *et al.*, "Plasmon lasers at deep subwavelength scale," Nature **461**, 629–632 (2009).
12. S. Jiang, Y. Zhang, and R. Zhang, *et al.*, "Distinguishing adjacent molecules on a surface using plasmon-enhanced Raman scattering," Nat. Nanotechnol. **10**, 865–869 (2015).
13. F. Benz, M. K. Schmidt, and A. Dreismann, *et al.*, "Single-molecule optomechanics in 'picocavities'," Science **354**, 726–729 (2016).
14. N. Chiang, X. Chen, and G. Goubert, *et al.*, "Conformational contrast of surface-mediated molecular switches yields angstrom-scale spatial resolution in ultrahigh vacuum tip-enhanced Raman spectroscopy," Nano Lett. **16**, 7774–7778 (2016).
15. M. H. Liao, S. Jiang, and C. R. Hu, *et al.*, "Tip-enhanced Raman spectroscopic imaging of individual carbon nanotubes with subnanometer resolution," Nano Lett. **16**, 4040–4046 (2016).
16. F. Wang and Y. R. Shen, "General properties of local plasmons in metal nanostructures," Phys. Rev. Lett. **97**, 206806 (2006).
17. H. Wu, Y. X. Gao, and P. Z. Xu, *et al.*, "Plasmonic nanolasers: pursuing extreme lasing conditions on nanoscale," Adv. Opt. Mater. **7**, 1900334 (2019).
18. H. Zhu, X. Yin, and L. Chen, *et al.*, "Directional beaming of light from a subwavelength metal slit with phase-gradient metasurfaces," Sci. Rep. **7**, 12098 (2017).
19. L. Yang, Z. K. Zhou, and H. Wu, *et al.*, "Generating a sub-nm-confined optical field in a nano-slit waveguiding mode," Adv. Photon. **5**, 046003 (2023).
20. H. Wu, L. Yang, and P. Z. Xu, *et al.*, "Photonic nanolaser with extreme optical field confinement," Phys. Rev. Lett. **129**, 013902 (2022).
21. Y. S. Hu, M. Zimmerley, and Y. Li, *et al.*, "Single-molecule superresolution light-sheet microscopy," ChemPhysChem **15**, 577–586 (2014).
22. Y. X. Zhao, M. Zhang, and W. T. Zhang, *et al.*, "Isotropic superresolution light-sheet microscopy of dynamic intracellular structures at subsecond timescales," Nat. Methods **19**, 359–369 (2022).
23. W. Wijngaard, "Guided normal modes of two parallel circular dielectric rods," J. Opt. Soc. Am. B **63**, 944–950 (1973).
24. C. S. Chang and H. C. Chang, "Vector normal modes on two-core optical fibers. I. The normal mode solutions," J. Lightwave Technol. **15**, 1213–1224 (1997).
25. F. L. Kien, L. Ruks, and S. N. Chormaic, *et al.*, "Spatial distributions of the fields in guided normal modes of two coupled parallel optical nanofibers," New J. Phys. **23**, 043006 (2021).
26. F. L. Kien, S. N. Chormaic, and T. Busch, "Optical force between two coupled identical parallel optical nanofibers," Phys. Rev. A **105**, 063517 (2022).
27. L. M. Tong, J. Y. Lou, and Z. Z. Ye, *et al.*, "Self-modulated taper drawing of silica nanowires," Nanotechnology **16**, 1445–1448 (2005).
28. L. M. Tong, L. L. Hu, and J. J. Zhang, *et al.*, "Photonic nanowires directly drawn from bulk glasses," Opt. Express **14**, 82–87 (2006).
29. J. Jackle and K. Kawasaki, "Intrinsic roughness of glass surfaces," J. Phys. Condens. Matter **7**, 4351–4358 (1995).
30. E. Radlein and G. H. Frischat, "Atomic force microscopy as a tool to correlate nanostructure to properties of glasses," J. Non-Cryst. Solids **222**, 69–82 (1997).
31. J. E. Hoffman, S. Ravets, and J. A. Grover, *et al.*, "Ultrahigh transmission optical nanofibers," AIP Adv. **4**, 067124 (2014).
32. R. Nagai and T. Aoki, "Ultra-low-loss tapered optical fibers with minimal lengths," Opt. Express **22**, 28427–28436 (2014).
33. N. Yao, S. Y. Linghu, and Y. X. Xu, *et al.*, "Ultra-long subwavelength micro/nanofibers with low loss," IEEE Photon. Technol. Lett. **32**, 1069–1072 (2020).
34. J. B. Zhang, Y. Kang, and X. Guo, *et al.*, "High-power continuous-wave optical waveguiding in a silica micro/nanofibre," Light Sci. Appl. **12**, 89 (2023).
35. F. Salvat-Pujol and J. S. Villarrubia, "Conventional vs. model-based measurement of patterned line widths from scanning electron microscopy profiles," Ultramicroscopy **206**, 112819 (2019).
36. T. Nakai, N. Norimatsu, and Y. Noda, *et al.*, "Changes in refractive index of fluoride glass fibers during fiber fabrication processes," Appl. Phys. Lett. **56**, 203–205 (1990).
37. H. Kakiuchida, K. Saito, and A. J. Ikushima, "Refractive index, density and polarizability of silica glass with various fictive temperatures," Jpn. J. Appl. Phys. **43**, L743–L745 (2004).
38. T. G. Tiecke, K. P. Nayak, and J. D. Thompson, *et al.*, "Efficient fiber-optical interface for nanophotonic devices," Optica **2**, 70–75 (2015).
39. E. P. S. Tan and C. T. Lim, "Mechanical characterization of nanofibers-a review," Compos. Sci. Technol. **66**, 1102–1111 (2006).
40. M. Asobe, T. Kanamori, and K. Kubodera, "Applications of highly nonlinear chalcogenide glass-fibers in ultrafast all-optical switches," IEEE J. Quantum Electron. **29**, 2325–2333 (1993).
41. Z. R. Li, C. F. Yao, and Z. X. Jia, *et al.*, "Broadband supercontinuum generation from 600 to 5400 nm in a tapered fluorotellurite fiber pumped by a 2010 nm femtosecond fiber laser," Appl. Phys. Lett. **115**, 091103 (2019).
42. P. Anger, P. Bharadwaj, and L. Novotny, "Enhancement and quenching of single-molecule fluorescence," Phys. Rev. Lett. **96**, 113002 (2006).
43. S. Kühn, U. Håkanson, and L. Rogobete, *et al.*, "Enhancement of single-molecule fluorescence using a gold nanoparticle as an optical nanoantenna," Phys. Rev. Lett. **97**, 017402 (2006).
44. B. N. J. Persson and A. Baratoff, "Inelastic electron tunneling from a metal tip: the contribution from resonant processes," Phys. Rev. Lett. **59**, 339–342 (1987).
45. Y. Yang, D. Zhu, and W. Yan, *et al.*, "A general theoretical and experimental framework for nanoscale electromagnetism," Nature **576**, 248–252 (2019).
46. L. Baschir, C. Opran, and D. Savastru, *et al.*, "Ellipsometric investigations of a-As_2S_3 thin films obtained by RF magnetron sputtering," Chalcogenide Lett. **15**, 199–205 (2018).
47. W. S. Rodney, I. H. Malitson, and T. A. King, "Refractive index of arsenic trisulfide," J. Opt. Soc. Am. B **48**, 633–636 (1958).
48. L. V. R. Marcos, J. I. Larruquert, and J. A. Mendez, *et al.*, "Self-consistent optical constants of SiO_2 and Ta_2O_5 films," Opt. Mater. Express **6**, 3622–3637 (2016).